Integrated silicon carbide modulator for CMOS photonics

Keith Powell[1,2], Liwei Li[1], Amirhassan Shams-Ansari[2], Jianfu Wang[1], Debin Meng[1], Neil Sinclair[2,3], Jiangdong Deng[4], Marko Lončar[2*] & Xiaoke Yi[1*]

Author affiliations. [1]School of Electrical and Information Engineering, the University of Sydney, NSW 2006, Australia. [2]John A. Paulson School of Engineering and Applied Sciences, Harvard University, Cambridge, MA 02138, USA. [3]Division of Physics, Mathematics and Astronomy, and Alliance for Quantum Technologies (AQT), California Institute of Technology, 1200 E. California Boulevard, Pasadena, CA 91125, USA. [4]Center for Nanoscale Systems, Harvard University, Cambridge, MA 02138, USA.
*E-mail: loncar@seas.harvard.edu; xiaoke.yi@sydney.edu.au

The electro-optic modulator encodes electrical signals onto an optical carrier, and is essential for the operation of global communication systems and data centers that society demands[1]. An ideal modulator results from scalable semiconductor fabrication and is integratable with electronics. Accordingly, it is compatible with complimentary metal-oxide semiconductor (CMOS) fabrication processes. Moreover, modulators using the Pockels effect enables low loss, ultrafast and wide-bandwidth data transmission. Although strained silicon-based modulators could satisfy these criteria, fundamental limitations such as two-photon absorption, poor thermal stability and a narrow transparency window hinder their performance. On the other hand, as a wide bandgap semiconductor matrial, silicon carbide is CMOS compatible and does not suffer from these limitations. Due to its combination of color centers, high breakdown voltage, and strong thermal conductivity, silicon carbide is a promising material for CMOS electronics and photonics with applications ranging from sensors to quantum and nonlinear photonics[2-4]. Importantly, silicon carbide exhibits the Pockels effect, but a modulator has not been realized since the discovery of this effect more than three decades ago. Here we design, fabricate, and demonstrate the first Pockels modulator in silicon carbide. Specifically, we realize a waveguide-integrated, small form-factor, gigahertz-bandwidth modulator that can operate using CMOS-level drive voltages on a thin film of silicon carbide on insulator. Furthermore, the device features no signal degradation and stable operation at high optical intensities (913 kW/mm²), allowing for high optical signal-to-noise ratios

for long distance communications. Our work unites Pockels electro-optics with a CMOS platform to pave the way for foundry-compatible integrated photonics.

The convergence of photonics and CMOS electronics empowers photonic integrated circuits to meet the ever-increasing demand for data throughput in information systems[5,6]. In particular, the electro-optic (EO) modulator is at the center of this convergence as a critical component for encoding electrical signals onto light for applications in datacenters, telecommunication networks and microwave photonic systems. State-of-the-art modulators based on silicon, the workhorse material of electronics, rely on the free carrier plasma dispersion effect. This effect is intrinsically absorptive and nonlinear as it causes coupled phase and amplitude modulation, which distorts the signal modulation amplitude and restrict usage of advanced modulation formats[7]. Alternatively, EO modulators based on the Pockels effect i.e. linear EO effect, which exists in non-centrosymmetric crystals, allows the refractive index to vary linearly and rapidly in proportion to an applied electric field. Consequently, Pockels modulators are exploited to achieve high data rates and conversion efficiencies without the addition of optical loss[8]. The Pockels effect is not present in most materials in the CMOS family, including silicon and silicon nitride. Aluminum nitride (AlN) exhibits the Pockels effect with non-equal EO tensors, and has relatively low refractive index, which increases the complexity in dense optoelectronic integration[9]. Modifications to the crystal symmetry of CMOS materials by strain have been proposed to realize EO modulators[10-12], but suffer from trade-offs fabrication complexity. For example, strained silicon[11,12] suffers from two-photon optical absorption and poor thermal stability that is inherent to silicon. Furthermore, the relatively small indirect bandgap of silicon prevents the usage of silicon waveguide in the visible spectrum range, which is of great interest for applications in sensing and quantum optics[13,14]. Commonly-used lithium niobate (LiNbO$_3$) Pockels modulators have a strong EO coefficient[15]. However, they suffer from signal-distortion induced by photorefraction that worsens with increasing optical powers[16], and is avoided by post-modulation amplification in applications. Moreover, low costs and high yields on chip are required, as permitted by the integration via CMOS compatible fabrication[17].

58   One CMOS-compatible material that exhibits the Pockels effect is silicon carbide (SiC)[18]. In

59   particular, the cubic (3C) polytype of SiC has the largest measured EO coefficient (~ 2.7 pm/V at 633

60   nm) of all SiC polytypes and has equal elements of the EO tensor[19], which simplifies optoelectronic

61   integration. Moreover, the wide bandgap of SiC allows broadband optical transparency from ultraviolet

62   to infrared. Despite this, a SiC-based Pockels modulator has not been experimentally demonstrated due

63   to poor crystal quality and difficulty obtaining low-loss waveguides[20–23]. Although 3C-SiC can be grown

64   directly onto a silicon substrate, it has been difficult to realize high-quality thin films, due to crystal

65   defects associated with this approach[23,24]. Wafer bonding techniques[25] and annealing processes[26] have

66   been explored to address these problems. Yet, the former demonstrates multimode waveguides while the

67   latter still results in a high (7 dB/cm) optical loss. These issues undermine a 3C-SiC Pockels modulator,

68   specifically one that features single-mode waveguides for stable and high extinction-ratio ring modulators

69   or quantum applications[27].

70   Moreover, due to its high electron mobility, as well as robust properties[27-30], SiC is a compelling

71   semiconductor material for next-generation CMOS electronics and a contender for realizing monolithic

72   integration of quantum and nonlinear photonics[2,3,27,31,32]. By taking the advantage of its high thermal

73   conductivity[33], wide band-gap, low thermo-optic coefficient[26] and high refractive index (~2.57)[34], SiC

74   offers the possibility of densely integrated and robust photonic devices with low fabrication costs via

75   CMOS-compatible nanofabrication[35] and the potential for integration with electronics.

76   Here we present the first SiC EO modulator. Optical modulation is achieved by electrically driving a

77   microring resonator in sub-micron-wide 3C-SiC on insulator waveguides via the Pockels effect. A

78   microring is chosen to enable a compact device footprint (90 μm^2), while maintaining high modulation

79   performance at low voltage. The modulator is fabricated with a CMOS-compatible process and operates

80   at a transmission rate of up to 15 gigabits per second using CMOS-level drive voltages. Importantly, we

81   reduce the impact of polycrystal grains and waveguide surface roughness to demonstrate ~5.4 dB/cm

82   optical loss using a single-mode waveguide. As a result of our work, we measure the Pockels coefficient

83 (1.5 pm/V) of 3C-SiC at an infrared wavelength for the first time. Moreover, the modulator is able to

84 operate continuously with high optical intensities of up to 913 kW/mm^2 without signal degradation,

85 facilitating low-noise microwave photonics[36] or parametric conversion of single photons[37].

86   The fabrication of the integrated 3C-SiC modulator begins with the 530 nm-thick SiC layer with a low

87 crystal defect density (see Methods) to reduce the scattering or absorption losses and increase EO

88 interaction. Figure 1a shows an optical micrograph of a fabricated modulator capable of operating using

89 a CMOS digital to analog converter (DAC). The modulator consists of a pair of 3C-SiC vertical grating

90 couplers (VGCs) as optical input and output ports, an optical waveguide ring resonator with a loaded

91 quality (Q_L) factor of 34,310 to balance modulation efficiency and bandwidth[38], and microwave strip line

92 electrodes to deliver electrical signals. The waveguides and the VGCs are structured by electron beam

93 lithography (EBL) (see Methods), in which a typical waveguide width of 800 nm is chosen to maintain

94 single mode operation with high optical mode confinement. The electrodes consist of a pair of ground

95 electrodes placed next to the sides of the waveguide and a signal electrode above the waveguide (Fig.1b).

96 A 1-µm-thick top cladding SiO2 layer is deposited to separate the electrode to the waveguide, which

97 prevents optical loss from mode interaction with the metal. Figure 1c shows a cross sectional scanning

98 electron micrograph (SEM) of the modulator to illustrate the geometries of the waveguide and electrodes.

99 The electrode thickness (~500 nm) is chosen to reduce radio frequency (RF) loss due to the skin effect.

100 As depicted in Fig. 1d, when a voltage is applied across the signal and ground electrodes, a vertical

101 electric field is induced predominantly in the vertical direction overlapping with the optical mode to probe

102 the Pockels effect. The ring cavity enables the phase change to be translated into an intensity modulated

103 output, where the resonant enhancement of the modulator allows for a small device footprint and low

104 drive voltage operation. Figure 1e shows a SEM of our etched waveguide, which can achieve a root-

105 mean-squared sidewall roughness less than 2.4 nm[26] facilitating absorption limited optical loss. To

106 qualify the optical loss, the optical spectrum of the microring resonator with critically coupled resonances

107 operating at the telecommunication wavelengths (1569 nm - 1600 nm) is measured to reveal single mode

108 operation (Fig. 1f) with a resonance linewidth of 36.9 pm (Fig. 1g). The obtained intrinsic Q (Q_I) is

109 86,000 corresponding to a linear propagation loss of ~5.4 dB/cm.

110 To characterize the maximum operational bandwidth of our fabricated modulator, we examine the EO

111 response at an optical input power of 6.8 mW (see Methods), which shows a 3 dB bandwidth of 7.1 GHz

112 (Fig. 2a). The bandwidth is limited by the cavity photon lifetime of 28 ps, calculated based on the

113 measured cavity linewidth (45 pm), that corresponds to the modulation bandwidth of around 5.7 GHz.

114 The electrode circuit of the modulator has much broader spectral response exceeding 30 GHz, as

115 indicated in the inset of Fig. 2a. Therefore, higher bandwidths could be achieved via reducing the cavity

116 Q factor, however this will result in a lower modulation index with the same RF signal strength[38].

117 To determine the EO performance of the modulator, we use light of 1544.1 nm wavelength and drive

118 the modulator with frequencies between 2.5 GHz and 17.5 GHz with a peak to peak drive voltage (Vpp)

119 of 1V (see Methods). The generation of double sidebands seen in the optical spectrum explicitly

120 demonstrates the resultant intensity modulation (Fig. 2b). For increasing frequency, a reduction in

121 sideband power is observed, consistent with the roll off induced by the resonant linewidth. For the

122 modulation frequency less than the resonator linewidth e.g. 2.5 GHz, the modulator can achieve an

123 extinction ratio of 3dB with Vpp = 8V. Using the measured optical spectrum and determining the electric

124 field strength inside the waveguide, we are able to extract the Pockels coefficient as 1.5 pm/V (see

125 Methods) which is higher than AlN (1pm/V)[9]. The combination with a low permittivity (~9.7)[39] and high

126 refractive index[34] also allows for more efficient utilization of the linear EO effect in 3C-SiC over other

127 materials, e.g. LiNbO3. With direct current (DC) voltages, a resonance shift of 0.11 pm/V (see Methods)

128 is measured which is lower than the measured RF shift likely due to shielding caused by trapped charges

129 in the silicon rich SiO_x layer. This could be avoided by annealing or using higher purity thermal oxide.

130 To quantify the performance of our modulator for data transmission, we demonstrate low voltage

131 operation with digital modulation (see Methods). Using a non-return-to-zero (NRZ) pseudo random bit

132 sequence (PRBS) of 2^7 bits, we drive the modulator directly from a CMOS DAC operating with a Vpp

133 ranging from 0.2 V to 2 V (Fig. 3a). Figure 3b shows the measured binary data over a period of 5 ns at a

134 data rate of 5 Gb/s, with an optical input power of 6.8mW using drive voltages of 2 Vpp and 1.2 Vpp,

135 showing that the modulator correctly modulates the light intensity according to the applied digital

136 sequence. Figure 3c shows the modulator operates at low drive voltages and an optical input power of

137 6.8 mW across a range of modulation speeds, with the eye-diagram quality (Q_E) factors greater than 2.7,

138 which lead to bit-error ratios (BERs) below the hard-decision forward error correction (HD-FEC) limit

139 (3.8×10^{-3})[40,41]. While the drive voltage is reduced from Vpp=2V to 1.2V, the modulator still maintains

140 an open 5Gb/s NRZ eye diagram, allowing for successful data transmission and detection. With Vpp = 2

141 V and an optical input power of 6.8 mW, the modulator supports bit rates up to 10 Gb/s, limited by the

142 cavity photon lifetime bandwidth (5.7 GHz).

143 The ability for modulator to handle high optical powers is important for enhancing signal to noise

144 ratio in the growing field of microwave photonic applications[4,36], as well as for quantum transduction[37]

145 and nonlinear photonics[27]. To quantify the operation at high and continuous optical intensities, we

146 measure the EO responses of the modulator with varied optical input power. The results are shown in

147 Fig. 4a, in which the optical intensity within the waveguide at the resonance wavelength is calculated

148 from the peak circulating power within the ring resonator[42]. It shows by increasing the optical intensity

149 from 254 kW/mm^2 to 913 kW/mm^2, the EO response is enhanced by 10.2 dB without evidence of signal

150 distortion. The observed eye diagrams (Fig. 4b) also exhibit enlarged openings at 15 Gb/s with increased

151 optical intensities, which shows improved modulation performance for digital signals and the ability to

152 reach larger bandwidths. Moreover, Fig. 4c shows at an optical intensity of 913 kW/mm^2, the Q_E factors

153 extracted from the measured eye diagrams for all data rates at Vpp = 2 V are over 2.7, confirming the

154 operation of the modulator at high optical intensities.

155 To distinguish SiC for optical and electrical integration, we compare the material parameters of several

156 EO modulator platform (Fig. 4d). The large thermal conductivity of 3C-SiC (490 W/(m·K)) that is almost

157 double that of AlN and more than 12 fold larger than LiNbO$_3$, together with the high Moh's hardness and

158 large Young's modulus, make the modulator unrivaled for high power EO applications and co-integration

159 with CMOS electronics. Furthermore, the ultra-high breakdown field of 3C-SiC (4 MV/cm) which is 18

160 fold higher than $LiNbO_3$ enables the possibility to integrate RF amplifiers on chip with the modulator,

161 and makes it resistant to electro-magnetic attacks from RF bursts. Moreover, the high radiation hardness

162 of SiC also presents advantages in harsh operating environments[29].

163   We demonstrate an integrated Pockels modulator in SiC with a drive voltage compatible with CMOS

164 electronics, a small device footprint, and continuous low-noise data modulation at high optical intensities.

165 The SiC EO modulator opens new opportunities for direct optoelectronic integration using CMOS

166 foundries with the benefit to various applications ranging from optical networks, chip scale interconnects,

167 RF and microwave photonics and quantum information. Our work constitutes an essential piece in the

168 vision of a thin film SiC platform consisting of monolithic integration of modulators, photodiodes,

169 quantum defects and protocols to realize on chip photonics. Finally, the ability to integrate with CMOS

170 electronics could inspire a new generation of integrated optoelectronic devices for photonic signal

171 processing, chip-chip or intra-chip interconnects ushering in a new era of optical based electronics.

172

173 **REFERENCES**

174 1.   Reed, G. T., Mashanovich, G., Gardes, F. Y. & Thomson, D. J. Silicon optical modulators. *Nat.*

175   *Photonics* **4**, 518–526 (2010).

176 2.   Lukin, D. M. *et al.* 4H-silicon-carbide-on-insulator for integrated quantum and nonlinear

177   photonics. *Nat. Photonics* **14**, 330–334 (2020).

178 3.   Anderson, C. P. *et al.* Electrical and optical control of single spins integrated in scalable

179   semiconductor devices. *Science* **366**, 1225–1230 (2019).

180 4.   Ghelfi, P. *et al.* A fully photonics-based coherent radar system. *Nature* **507**, 341–345 (2014).

181 5.   Xu, Q., Schmidt, B., Pradhan, S. & Lipson, M. Micrometre-scale silicon electro-optic modulator.

182   *Nature* **435**, 325–327 (2005).

183   6.   Towards systems-on-a-chip. *Nat. Photonics* **12**, 311 (2018).

184   7.   Reed, G. T. *et al.* Recent breakthroughs in carrier depletion based silicon optical modulators.

185   *Nanophotonics* **3**, 229–245 (2014).

186   8.   Boyd, R. W. *Nonlinear Optics*. (Academic, Cambridge, 2003).

187   9.   Xiong, C., Pernice, W. H. P. & Tang, H. X. Low-loss, silicon integrated, aluminum nitride

188   photonic circuits and their use for electro-optic signal processing. *Nano Lett.* **12**, 3562–3568

189   (2012).

190   10.   Alexander, K. *et al.* Nanophotonic Pockels modulators on a silicon nitride platform. *Nat.*

191   *Commun.* **9**, 1–6 (2018).

192   11.   Jacobsen, R. S. *et al.* Strained silicon as a new electro-optic material. *Nature* **441**, 199–202

193   (2006).

194   12.   Berciano, M. *et al.* Fast linear electro-optic effect in a centrosymmetric semiconductor.

195   *Commun. Phys.* **1**, 1–9 (2018).

196   13.   Awschalom, D.D., Hanson, R., Wrachtrup, J. *et al.* Quantum technologies with optically

197   interfaced solid-state spins. *Nat. Photonics* **12**, 516–527 (2018).

198   14.   Aharonovich, I., Englund, D. & Toth, M. Solid-state single-photon emitters. *Nat.*

199   *Photonics* **10**, 631–641 (2016).

200   15.   Wang, C. *et al.* Integrated lithium niobate electro-optic modulators operating at CMOS-

201   compatible voltages. *Nature* **562**, 101–104 (2018).

202   16.   Jiang, H. *et al.* Fast response of photorefraction in lithium niobate microresonators. *Opt. Lett.* **42**,

203   3267–3270 (2017).

204   17.   Safian, R., Teng, M., Zhuang, L. & Chakravarty, S. Foundry-compatible thin film lithium

205   niobate modulator with RF electrodes buried inside the silicon oxide layer of the SOI wafer. *Opt.*

206   *Express* **28**, 25843–25857 (2020).

207   18.   Tang, X., Irvine, K. G., Zhang, D. & Spencer, M. G. Linear electro-optic effect in cubic silicon

208   carbide. *Appl. Phys. Lett.* **59**, 1938–1939 (1991).

209   19.   Barrios, C. A., Thomas, C. I., Spencer, M. & Lipson, M. 3C-SiC modulator for high-speed

210   integrated photonics. *Materials Research Society Symposium - Proceedings* **799**, 158–162

211   (2003).

212   20.   Vonsovici, A., Reed, G. T. & Evans, A. G. R. β-SiC-on insulator waveguide structures for

213   modulators and sensor systems. *Mater. Sci. Semicond. Process.* **3**, 367–374 (2000).

214   21.   Liu, Y. M. & Prucnal, P. R. Low-loss silicon carbide optical waveguides for silicon-based

215   optoelectronic devices. *IEEE Photonics Technol. Lett.* **5**, 704–707 (1993).

216   22.   Reed, G. T. *et al.* Fabrication and evaluation of SiC optical modulators. *Silicon-based Hybrid*

217   *Optoelectron. IV* **4654**, 145–156 (2002).

218   23.   Cardenas, J. *et al.* High Q SiC microresonators. *Opt. Express* **21**, 16882–16887 (2013).

219   24.   Lu, X., Lee, J. Y., Feng, P. X.-L. & Lin, Q. High Q silicon carbide microdisk resonator. *Appl.*

220   *Phys. Lett.* **104**, 181103 (2014).

221   25.   Fan, T., Moradinejad, H., Wu, X., Eftekhar, A. A. & Adibi, A. High-Q integrated photonic

222   microresonators on 3C-SiC-on-insulator (SiCOI) platform. *Opt. Express* **26**, 25814–25826

223   (2018).

224   26.   Powell, K. *et al.* High-Q suspended optical resonators in 3C silicon carbide obtained by thermal

225   annealing. *Opt. Express* **28**, 4938–4949 (2020).

226   27.   Lukin, D. M., Guidry, M. A. & Vučković, J. Integrated quantum photonics with silicon carbide:

227   challenges and prospects. *PRX Quantum* **1**, 020102 (2020).

228   28.   Atatüre, M., Englund, D., Vamivakas, N., Lee, S. Y. & Wrachtrup, J. Material platforms for

229   spin-based photonic quantum technologies. *Nat. Rev. Mater.* **3**, 38–51 (2018).

230   29.   Lee, T. H., Bhunia, S. & Mehregany, M. Electromechanical computing at 500°C with silicon

231   carbide. *Science* **329**, 1316–1318 (2010).

232   30.   Nakamura, D. *et al*. Ultrahigh-quality silicon carbide single crystals. *Nature* **430**, 1009–1012

233   (2004).

234   31   Gordon, L., Janotti, A. & Van de Walle, C.G. Defects as qubits in 3C- and 4H-SiC. *Physical*

235   *Review B* **92**, 045208 (2015).

236   32.   Whiteley, S. J. *et al*. Spin–phonon interactions in silicon carbide addressed by Gaussian

237   acoustics. *Nat. Phys.* **15**, 490–495 (2019).

238   33.   Yamaoka, S. *et al.* Directly modulated membrane lasers with 108 GHz bandwidth on a high-

239   thermal-conductivity silicon carbide substrate. *Nat. Photonics* **15**, 28–35 (2021).

240   34.   Tropf, W. J., Thomas, M. E. & Linevsky, M. J. Infrared refractive indices and thermo-optic

241   coefficients for several materials. *Optical Diagnostic Methods for Inorganic Transmissive*

242   *Materials* **3425**, 160–171 (1998).

243   35.   Nabki, F., Dusatko, T. A., Vengallatore, S. & El-Gamal, M. N. Low-stress CMOS-compatible

244   silicon carbide surface-micromachining technology-part I: Process development and

245   characterization. *J. Microelectromechanical Syst.* **20**, 720–729 (2011).

246   36.   Marpaung, D., Yao, J. & Capmany, J. Integrated microwave photonics. *Nat. Photonics* **13**, 80–

247   90 (2019).

248   37.   Holzgrafe, J. *et al*. Cavity electro-optics in thin-film lithium niobate for efficient microwave-to-

249   optical transduction. *Optica* **7**, 1714–1720 (2020).

250   38.   Yu, H. *et al*. Trade-off between optical modulation amplitude and modulation bandwidth of

251   silicon micro-ring modulators. *Opt. Express* **22**, 15178–15189 (2014).

252   39.   Patrick, L. & Choyke, W. J. Static dielectric constant of SiC. *Physical Review B* **2**, 2255–2256

253   (1970).

254   40.   Cho, J., Xie, C. & Winzer, P.J. Analysis of soft-decision FEC on non-AWGN channels. *Opt.*

255   *Express* **20**, 7915–7928 (2012).

256   41.   Asif, R. Advanced and flexible multi-carrier receiver architecture for high-count multi-core fiber

257   based space division multiplexed applications. *Sci. Rep.* **6**, 27465 (2016).

258   42.   Ikeda, K., Saperstein, R. E., Alic, N. & Fainman, Y. Thermal and Kerr nonlinear properties of

259   plasma-deposited silicon nitride/ silicon dioxide waveguides. *Opt. Express* **16**, 12987–12994

260   (2008).
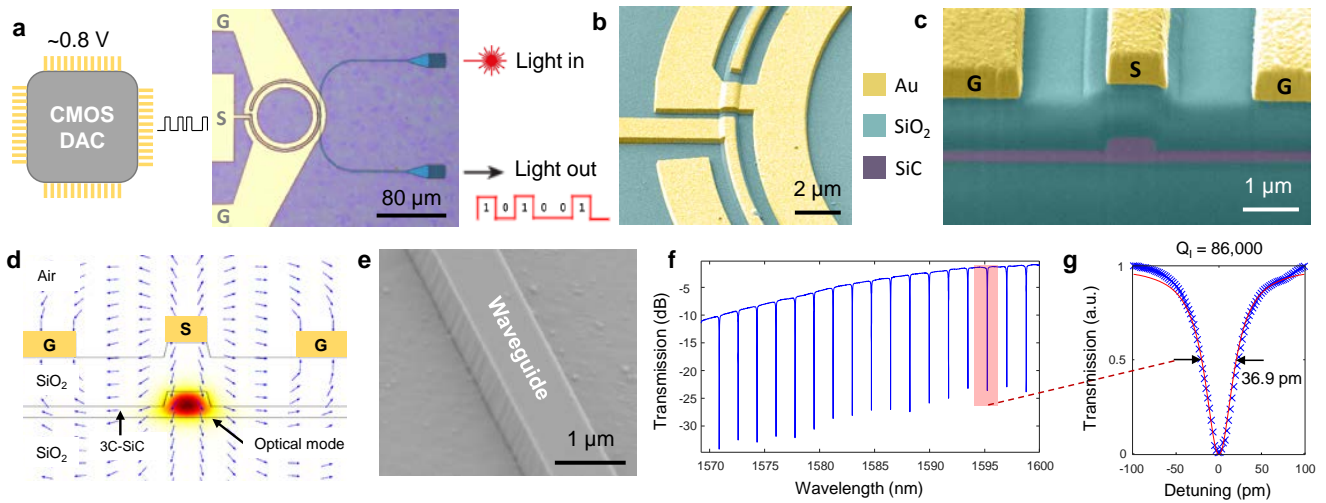
Fig. 1 Integrated Pockels modulator in SiC on insulator. (a) Overview of the fabricated ring modulator showing compatibility with CMOS voltages. (b) False color SEM of the microring waveguide and modulator electrodes. (c) False color SEM cross-section of the active region of the modulator. (d) Simulated static electric field and optical mode of the active region of the modulator. (e) SEM of an etched waveguide with the sidewall shown. (f) Measured optical spectrum of the microring resonator. (g) Lorentz fit of the resonance lineshape to determine the intrinsic optical quality (Q_I) factor. (Cross: Measurement; Solid line: Lorentz fitting)
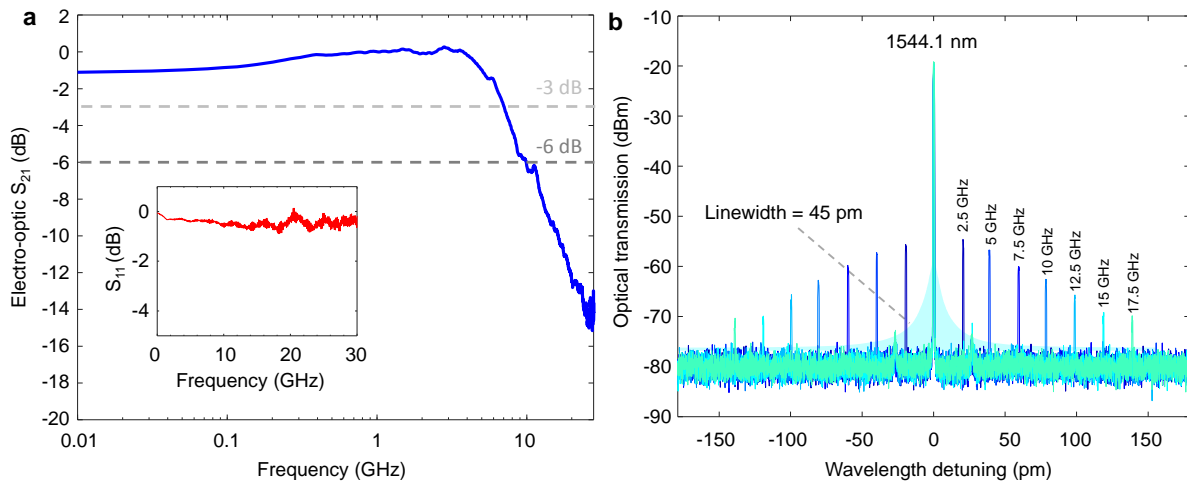
Fig. 2 Modulator bandwidth and EO characterization. (a) RF s-parameter characterization featuring a -3dB and -6dB bandwidths of 7.1 GHz and 9.9 GHz respectively. S_{21}, transmission coefficient of the scattering matrix. Inset shows the S_{11}, reflection spectrum of the modulator. (b) Optical spectrum at the output of the modulator for various input RF frequencies. The measurement at 2.5GHz which is within the resonator linewidth is used in the Pockels coefficient extraction.
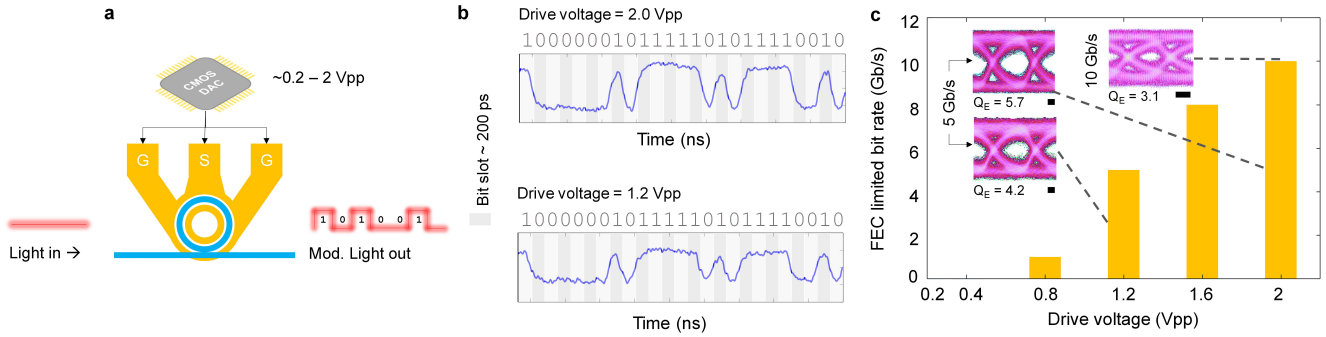
Fig 3. Digital CMOS level electro-optic modulation with NRZ PRBS of 2^7 bits. (a) Setup configuration using a CMOS DAC to drive the ground-signal-ground (GSG) electrodes of the modulator. (b) Time domain waveforms measured at the output of the modulator at 5 Gb/s for drive voltages of 2 Vpp and 1.2 Vpp respectively. (c) Drive-voltage-dependent eye-diagram quality (Q_E) factors for increasing bit rat. The Q_E factor greater than 2.7 corresponds to BER below the HD-FEC limit. Scale bars, 33 picoseconds.
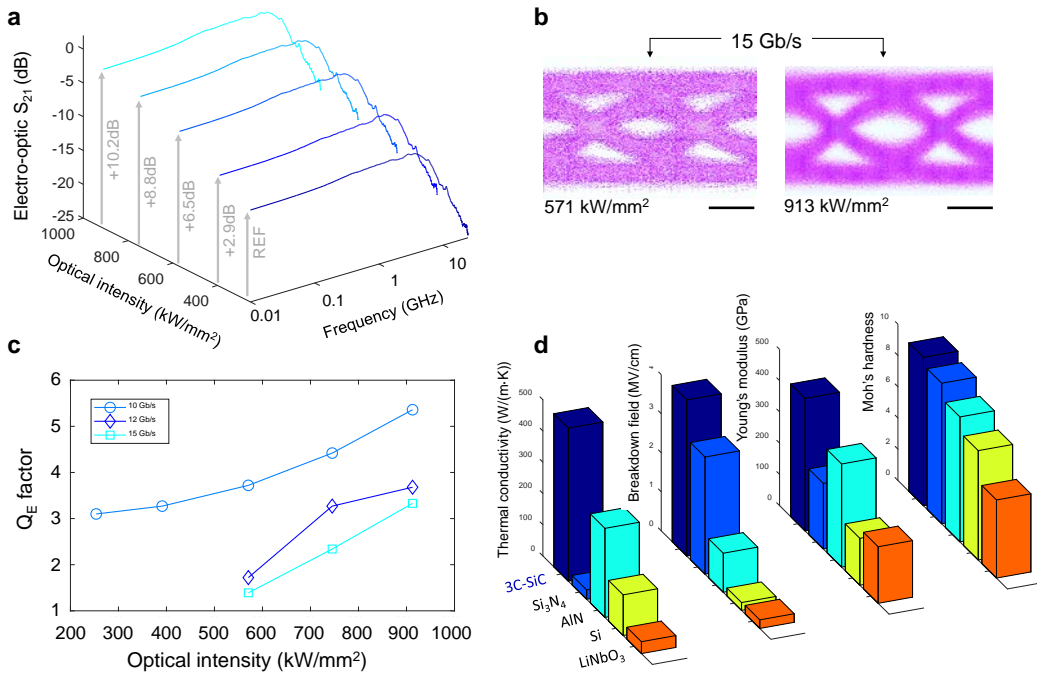
Fig 4. High power operation. (a) Electro-optic s-parameter characterization at high optical intensities showing an improvement in RF responses. (b) Measured eye diagrams at 15 Gb/s confirming the operation of the modulator at high optical intensities. (c) Q_E factors as a function of optical intensity for bit rates of 10 Gb/s, 12 Gb/s and 15 Gb/s showing an improved modulation performance for higher input intensity. (d) Material parameter comparison of 3C-SiC with widely used optical materials showing the distinct advantages of SiC for high power handling. Scale bars, 33 picoseconds.

Author contributions. K. P., M. L. and X. Y. conceived the experiment. K. P., L. L., A. S. and J. D. fabricated the devices. J. W. and D. M. performed numerical simulations. K. P., L. L., J. D. and N. S. carried out the device characterization. K. P., N.S. and X. Y. wrote the manuscript with contribution from all authors. M. L. and X. Y. supervised the project.

Competing interests. None.

Correspondence and requests for materials should be addressed to X. Y.

METHODS

Device fabrication. Devices are fabricated from a commercially available 3C-SiC on silicon wafer with 3.5 μm of SiC epitaxially grown on a silicon substrate supplied by NOVASiC. A 2 μm thick low pressure chemical vapor deposition (LPCVD) SiO_2 is deposited onto the SiC thin film, and the resultant stack is Van der Waals bonded to a thermal SiO_2 on silicon wafer before thinning down SiC via an inductive coupled plasma reactive ion etching (ICP-RIE) process. The device consists of a thin 3C-SiC layer, LPCVD SiO_2 and a silicon substrate for the handle. The waveguides and grating couplers are patterned on 2 μm of hydrogen silsesquioxane (FOX-16) resist using EBL. They are subsequently etched into the SiC layer using an ICP-RIE process consisting of the CMOS foundry compatible gases SF_6 and C_4F_8[26]. The built-up polymer due to C_4F_8 etch gas is removed using a two-step wet cleaning process. First, a solution of hydrogen peroxide and ammonium hydroxide is used to remove the polymer. Second, a solution of hydrogen peroxide and hydrochloric acid is used to remove the metal ions from the surface of the etched waveguides. Plasma enhanced chemical vapor deposition (PECVD) process is used to deposit a 1 μm layer of SiO_2 onto the fabricated devices to act as an insulation layer between the electrodes and the device, which is sufficiently thick to minimize excess absorption due to the metal electrodes. Device electrodes fabrication involves EBL patterning on Polymethyl methacrylate resist, developed with a mixed solution of 1 part Methyl isobutyl ketone and 3 parts Isopropyl alcohol. Metal layers consisting of 5 nm titanium and 500 nm of gold are deposited using electron beam evaporation followed by lift-off using a solution of N-Methyl-2-pyrrolidone.

Electro-optic characterization and transmission spectrum measurement. Laser light (Keysight 81960A) around 1550 nm is amplified using an erbium doped fiber amplifier (EDFA) followed by an optical bandpass filter to reduce amplified spontaneous emission (ASE) noise. The resultant light is launched into the ring modulator (Extended Data Fig. 1a). The laser is tuned to a wavelength that matches

338   the most linear edge of a resonance to ensure minimal distortion in the modulated signal. A second EDFA

339   is placed after the modulator to compensate for optical loss before the optical to electrical conversion via

340   a 20 GHz photodetector (Discovery). A high-speed microwave probe (GGB) is used to deliver the

341   modulation signal to the input port of the transmission line. To measure the EO response, the sinusoidal

342   signal with sweeping frequency from a signal generator of a vector network analyzer (VNA, Keysight

343   N5234A) is used to drive the modulator via the microwave probe, while the photodetector output is

344   connected with the VNA receiver. EO response is obtained from the s-parameter of the VNA, where RF

345   cable losses are calibrated out of the measured frequency responses. To measure the high-speed data

346   modulation, electrical PRBS signals of voltage varied from 0.2 Vpp to 2 Vpp are generated from a 65

347   GS/s arbitrary waveform generator (AWG, Keysight M8195A) and then connected with the microwave

348   probe (Extended Data Fig. 1b). A real-time digital sampling oscilloscope with an analogue bandwidth of

349   110 GHz (Keysight UXR series) is used to capture the received signal from the photodetector. The

350   oscilloscope acts as the receiver for the PRBS, where a second-order phase locked loop is used for clock

351   recovery to generate an eye diagram of the received data. The eye Q_E factor was measured directly from

352   the oscilloscope using persistence mode for a fixed number of waveforms.

353   By scanning the wavelength of the tunable laser and detecting the optical power (Keysight N7744A) at

354   the optical output of the modulator, the transmission spectra for different DC voltages are obtained. DC

355   bias voltages from -20V to +20V are applied on the modulator ground-signal-ground electrodes, and the

356   results are shown in Extended Data Fig. 2.

357   **Pockels coefficient extraction.** Finite element method solver (COMSOL Multiphysics) is used to

358   simulate the optical mode profile and the electric field distribution inside the SiC waveguide. The electro-

359   optic overlap integral is numerically calculated to evaluate the interaction of optical and electric fields[43].

360   The modulation index is determined using the Jacobi-anger expansion method which is obtained from

361   the optical power ratio of the modulated sideband and the optical carrier. The voltage induced effective

index change of the fundamental transverse electric mode is calculated from the measured resonance shift, and then the EO coefficient of the 3C-SiC waveguide at the operating wavelength is derived correspondingly[38,44].

Material parameter comparison. Extended Data Table 1 lists the comparison of common photonic integration materials with 3C-SiC, specifically parameters related to power handling of the modulator. The Young's modulus and Moh's hardness are useful parameters for a broad range of applications. Moreover, the refractive index and electrical permittivity are also listed. Low electrical permittivity combined with a higher refractive index are favorable for a larger modulation efficiency at a given EO coefficient.

Data availability. The data sets generated and/or analysed during the current study are available from the corresponding authors on reasonable request.

43. Rao, A. & Fathpour, S. Compact lithium niobate electrooptic modulators. *IEEE Journal of Selected Topics in Quantum Electronics* **24,** 1-14 (2017).

44. Tazawa, H. *et al.* Ring resonator-based electrooptic polymer traveling-wave modulator. *J. Light. Technol.* **24**, 3514-3519 (2006).

45. Bhatnagar, M. & Baliga, B. J. Comparison of 6H-SiC, 3C-SiC, and Si for power devices. *IEEE Trans. Electron Devices* **40**, 645–655 (1993).

46. Guarino, A., Poberaj, G., Rezzonico, D., Degl'Innocenti, R. & Günter, P. Electro-optically tunable microring resonators in lithium niobate. *Nat. Photonics* **1**, 407–410 (2007).

47. Zhu, S. & Lo, G.-Q. Aluminum nitride electro-optic phase shifter for backend integration on silicon. *Opt. Express* **24**, 12501–12506 (2016).

48. Gao, Y., Tao, L., Tsang, H. K. & Shu, C. Graphene-on-silicon nitride waveguide photodetector with interdigital contacts. *Appl. Phys. Lett.* **112**, 211107 (2018).

385   49.   Lee, Y. S. *et al.* Hybrid Si-LiNbO$_3$ microring electro-optically tunable resonators for active

386   photonic devices. *Opt. Lett.* **36**, 1119–1121 (2011).

387   50.   Li, H. H. Refractive index of silicon and germanium and its wavelength and temperature

388   derivatives. *J. Phys. Chem. Ref. Data* **9**, 561–658 (1980).

389   51.   Arbabi, A. & Goddard, L. L. Measurements of the refractive indices and thermo-optic

390   coefficients of Si$_3$N$_4$ and SiO$_x$ using microring resonances. *Opt. Lett.* **38**, 3878–3881 (2013).

391   52.   Goel, S., Luo, X., Reuben, R. L. & Rashid, W. Bin. Atomistic aspects of ductile responses of

392   cubic silicon carbide during nanometric cutting. *Nanoscale Res. Lett.* **6**, 589 (2011).

393   53.   Arizmendi, L. Photonic applications of lithium niobate crystals. *Physica Status Solidi (A)*

394   *Applied Research* **201**, 253–283 (2004).

395   54.   Yushkov, Y., Oks, E., Zolotukhin, D. & Tyunkov, A. Properties of Thermo-Conductive

396   Ceramic-Based Coatings Deposited Using Fore-Vacuum Plasma-Cathode Electron Source. *7th*

397   *International Congress on Energy Fluxes and Radiation Effects (EFRE)*, 844–847 (IEEE, 2020).

398   55.   Wang, D., Wang, Z., Wang, Z., Qian, G. & Gong, X. Study on hydrocyclone separation

399   enhancement of micro Si/SiC from silicon-sawing waste by selective comminution. *Sep. Sci.*

400   *Technol.* 1–9 (2020).

401   56.   Moskalewicz, T. *et al.* Electrophoretic deposition and microstructure development of

402   Si3N4/polyetheretherketone coatings on titanium alloy. *Surf. Coatings Technol.* **350**, 633–647

403   (2018).

404   57.   Weitzel, C. E. *et al.* Silicon carbide high-power devices. *IEEE Trans. Electron Devices* **43**,

405   1732–1741 (1996).

406   58.   Stanicki, B. J. *et al.* Surface domain engineering in lithium niobate. *OSA Contin.* **3**, 345–358

407   (2020).

408   59.   Lu, X., Moille, G., Rao, A., Westly, D. A. & Srinivasan, K. Efficient photoinduced second-

409   harmonic generation in silicon nitride photonics. *Nat. Photonics* (2020).

410   60.   Liu, X. *et al.* Highly efficient Thermo-optic Tunable Micro-ring Resonator based on thin film

411   lithium niobate platform. *Opt. Lett.* **45**, 6318–6321 (2020).

412   61.   Qiu, C. *et al.* All-optical control of light on a graphene-on-silicon nitride chip using thermo-optic

413   effect. *Sci. Rep.* **7**, 1–7 (2017).

414   62.   Wang, C., Zhang, M., Stern, B., Lipson, M. & Lončar, M. Nanophotonic lithium niobate electro-

415   optic modulators. *Opt. Express* **26**, 1547–1555 (2018).

416   63.   Watanabe, N., Kimoto, T. & Suda, J. The temperature dependence of the refractive indices of

417   GaN and AlN from room temperature up to 515 °c. *J. Appl. Phys.* **104**, 106101 (2008).

418   64.   Komma, J., Schwarz, C., Hofmann, G., Heinert, D. & Nawrodt, R. Thermo-optic coefficient of

419   silicon at 1550 nm and cryogenic temperatures. *Appl. Phys. Lett.* **101**, 041905 (2012).

420   65.   Jackson, K. M., Dunning, J., Zorman, C. A., Mehregany, M. & Sharpe, W. N. Mechanical

421   properties of epitaxial 3C silicon carbide thin films. *J. Microelectromechanical Syst.* **14**, 664–

422   672 (2005).

423   66.   Jiang, W. C. & Lin, Q. Chip-scale cavity optomechanics in lithium niobate. *Sci. Rep.* **6**, 36920

424   (2016).

425   67.   Xiong, C. *et al.* Aluminum nitride as a new material for chip-scale optomechanics and nonlinear

426   optics. *New J. Phys.* **14**, 095014 (2012).

427   68.   Han, S., Seok, T. J., Quack, N., Yoo, B. W. & Wu, M. C. Large-scale silicon photonic switches

428   with movable directional couplers. *Optica* **2**, 370–375 (2015).

429   69.   Xiong, W. *et al.* SiNx films and membranes for photonic and MEMS applications. *J. Mater. Sci.*

430   *Mater. Electron.* **31**, 90–97 (2020).
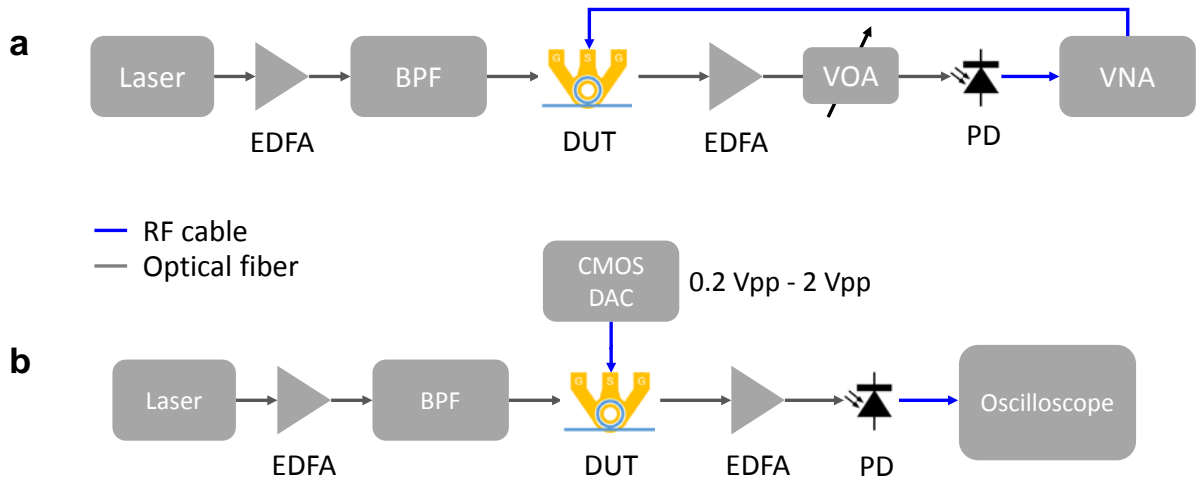
Extended Data

Extended Data Fig. 1 High speed measurement setups (a) Setup for measuring the EO response of the SiC modulator (b) Setup for testing the digital communications operation of the SiC modulator. EDFA, erbium doped amplifier; BPF, bandpass filter; DUT, device under test; VOA, variable optical attenuator; PD, photodiode; VNA, vector network analyzer.
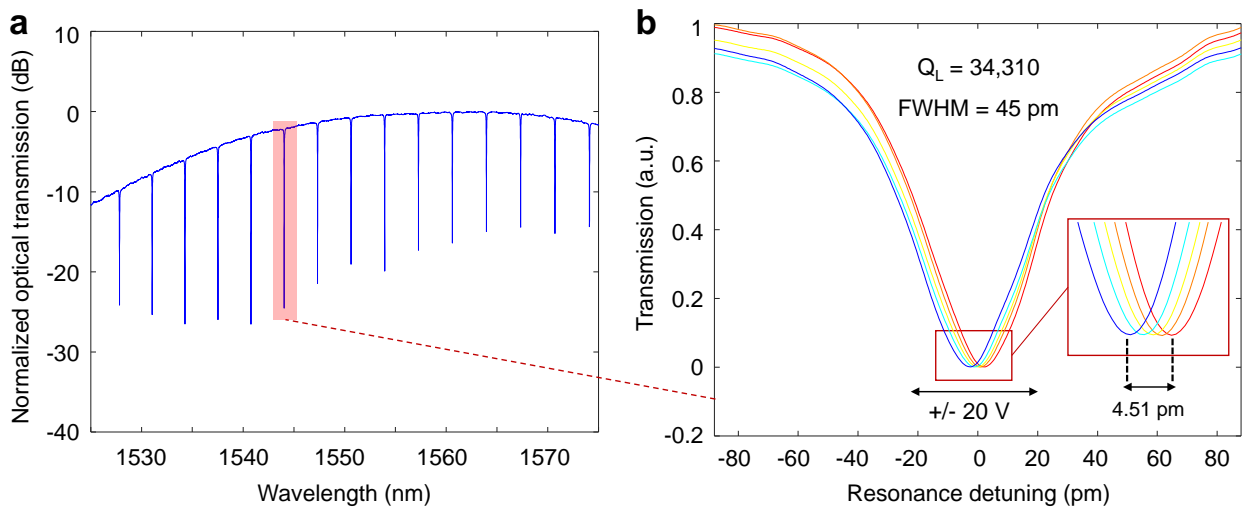
Extended Data Fig. 2. Optical characterization of the electro-optic ring modulator (a) optical transmission spectrum showing single mode operation (b) Measured DC electro-optic resonance detuning and the loaded quality (Q_L) factor of the modulator ring resonator over a DC voltage range of +/- 20 V. FWHM, full-width-half-maximum.

Extended Data Table 1 | Comparison of photonic integration platforms for power handling and robustness

	3C-SiC	LiNbO$_3$	AlN	Si	Si$_3$N$_4$
Relative permittivity	9.66 [45]	28 [46]	10 [47]	11.8 [45]	5.5 [48]
Refractive Index @ 1550 nm	2.57 [34]	n_o = 2.21 [49] n_e = 2.14	2.12 [9]	3.48 [50]	1.98 [51]
Moh's Hardness	9.5 [52]	5 [53]	8 [54]	7 [55]	9 [56]
Breakdown field	4 MV/cm [57]	220 kV/cm [58]	1 MV/cm [9]	200 kV/cm [45]	3 MV/cm [59]
Thermal conductivity	490 W/(m·K) [45]	38 W/(m·K) [60]	285 W/(m·K) [9]	130 W/(m·K) [9]	30 W/(m·K) [61]
Thermo-optic coefficient	5.8×10^{-5} K^{-1} [26]	3.9×10^{-5} K^{-1} [62]	2.3×10^{-5} K^{-1} [63]	1.8×10^{-4} K^{-1} [64]	2.5×10^{-5} K^{-1} [61]
Mechanical elastic/Young's modulus	424 GPa [65]	181 GPa [66]	330 GPa [67]	150 GPa [68]	210 GPa [69]

447
448
449
450
451
452